Climate Dynamics (2019) 52:3079–3098
https://doi.org/10.1007/s00382-018-4316-y

Improved seasonal predictive skill and enhanced predictability of the Asian summer monsoon rainfall following ENSO events in NCEP CFSv2 hindcasts

Chul-Su Shin[1] · Bohua Huang[1] · Jieshun Zhu[2,3] · L. Marx[1] · James L. Kinter III[1]

Received: 3 April 2018 / Accepted: 13 June 2018 / Published online: 19 June 2018

Abstract
The dominant modes of the Asian summer monsoon (ASM) rainfall variability, as well as their seasonal predictive skill and predictability, are investigated using two sets of seasonal hindcasts made with the NCEP Climate Forecast System (CFSv2): one from the NCEP CFS Reanalysis and Reforecast Project (CFS_RR) and the other using a Multi-ocean Analyses Ensemble initialization scheme (CFS_MAE). The 1st and 2nd empirical orthogonal function (EOF) modes of the observed ASM rainfall anomalies correspond respectively to the contemporaneous and delayed responses to El Niño and the Southern Oscillation (ENSO) in its developing and decaying years. In general, CFSv2 is capable of skillfully predicting these two dominant ASM modes on the seasonal time scale up to 5 months in advance. Moreover, the predictive skill of the ASM rainfall in CFS_MAE is much higher with respect to the delayed ENSO mode than the contemporaneous one. The predicted principal component of the former maintains high correlation skill and small ensemble spread about two seasons ahead while the latter is significantly degraded in both measures after one season. A maximized signal-to-noise EOF analysis further shows that the delayed ASM response to ENSO is also the most predictable pattern at long leads in CFS_RR. The improved predictive skill of the ASM rainfall following ENSO events originates from the enhanced predictability associated with the active air-sea feedback in the Indo-northwestern Pacific domain from the ENSO peak to the ENSO demise phase, which are well captured in the CFSv2 hindcasts.

Keywords Asian summer monsoon · CFSv2 hindcasts · Contemporaneous and delayed responses to ENSO · Seasonal prediction and predictability

1 Introduction

The Asian summer monsoon (ASM) rainfall supports ecosystems and human lives in this densely populated region by being a source of abundant water. The ASM rainfall exhibits large year-to-year variations, and unusual anomalous rainfall often leads to many weather or climate extreme events such as floods and droughts. Therefore, better seasonal prediction of the anomalous monsoon rainfall can have a great impact on the lives and livelihoods in many Asian countries and has long been a challenging topic in both academic research groups and operational prediction centers (e.g., Shukla 1987; Webster et al. 1998).

It has been recognized that El Niño and the Southern Oscillation (ENSO) is one of the main influencing factors on the interannual variability of the ASM rainfall and the ASM response to ENSO varies in the different phase of the ENSO cycle (e.g., Webster and Yang 1992; Lau and Nath

Electronic supplementary material The online version of this article (https://doi.org/10.1007/s00382-018-4316-y) contains supplementary material, which is available to authorized users.

✉ Chul-Su Shin
cshin3@gmu.edu

[1] Department of Atmospheric, Oceanic and Earth Sciences and Center for Ocean-Land-Atmosphere Studies, George Mason University, 4400 University Drive, Fairfax, VA 22030, USA

[2] Climate Prediction Center, National Centers for Environmental Prediction/NOAA, College Park, MD, USA

[3] Earth System Science Interdisciplinary Center, University of Maryland, College Park, MD, USA

2000; Wang et al. 2000, 2003, 2017; Lau et al. 2004; Yang and Lau 2006; Yang and Jiang 2014; Xie et al. 2016; among others). Relationship between the ASM rainfall variability and the evolving ENSO with time have been studied primarily on regional scales, such as the monsoons in India, East Asia, South China Sea (SCS), and northwestern Pacific (NWP). For instance, many previous studies suggested that the shift of the atmospheric deep convection center from the western to the central tropical Pacific in the El Niño developing summer often results in suppressed rainfall over India (e.g., Shukla and Paolino 1983; Webster and Yang 1992). It is debatable on whether the relationship between ENSO and the Indian monsoon is weakening or evolving. Some studies (e.g., Kumar et al. 1999; Kinter et al. 2002; Rajeevan et al. 2012) showed weakened correlations between the ENSO and monsoon indices in recent decades, while others argued that the relationship has not changed if different measures are used (e.g., Kumar et al. 2006; Xavier et al. 2007). Recently, Cash et al. (2017) found that the range of the correlations between the Indian monsoon and ENSO using the historical data is within a reasonable estimate of sampling variation.

On the other hand, many studies examined the delayed ASM response on regional scales to ENSO during its decaying phase, with an emphasis on the East Asian monsoon at first. For example, enhanced anomalous rainfall has been reported near the Yangtze River in China during summer following El Niño events (e.g., Wu et al. 2003; Huang et al. 2004; Zhang et al. 2016). Compared with the earlier period (late 1950–1979s), this delayed relationship between the summer monsoon and ENSO has been stronger in the period 1980-early 2000s in the East Asian and NWP monsoon regions (Yun et al. 2010; Wu et al. 2012) as well as the northern Australia-Indonesia monsoon region (Wang et al. 2008). More recently, Chowdary et al. (2017) showed that the Indian summer monsoon rainfall variability during the El Niño decaying phase is strongly dependent upon the timing of El Niño with respect to the boreal summer season (i.e., early decay, decay by mid-summer, or no decay in summer). Wang et al. (2017) also pointed out that different intensities and evolutions of El Niño events can give rise to the uncertainty of the East Asian monsoon rainfall response in the subsequent boreal summer.

Since the beginning of the 21st century, substantial efforts have been made to evaluate and improve seasonal prediction of the ASM rainfall as a whole and associated atmospheric circulations in operational coupled ocean–atmosphere seasonal prediction systems (e.g., Kim et al. 2012) and in hindcasts by individual models (e.g., Yang et al. 2008; Liang et al. 2009; Jiang et al. 2013; Zuo et al. 2013) as well as multiple models with large ensemble members (e.g., Kang et al. 2002; Wang et al. 2004, 2005, 2009; Kumar et al. 2005; Chowdary et al. 2010; Li et al. 2012). As a result, it is commonly held that state-of-the-art climate models are capable of predicting key features of the ASM variability. In particular, Liang et al. (2009) and Zuo et al. (2013) reported that the ASM rainfall anomalies are predictable in both the developing and decaying phases of ENSO with different patterns, based on the hindcasts from the National Centers for Environment Prediction (NCEP) Climate Forecast System (CFS).

Figure 1 Shows the seasonal prediction skill and root-mean-square error of the June–September (JJAS) mean rainfall anomalies for 1979–2008 using CFSv2 hindcasts initialized with four different ocean analyses (see Sect. 2 for more details) at 1-month lead (starting from early May) and 5-month lead (starting from early January). It is impressive that the skill of the 5-month lead forecast (right panels of Fig. 1) is generally comparable to that of the 1-month lead forecast (left panels of Fig. 1), although lower skill and larger error appear over the southwest-northeast oriented regions from the southeast Indian Ocean (IO) to Malaysia in the 5-month lead prediction. Under what conditions can the seasonal prediction skill remain as high for about two seasons as it is at short leads? This is a main motivation for this study.

We examine the seasonal predictive skill of the ASM rainfall using two independent seasonal hindcasts using NCEP CFS version 2 (CFSv2); one set is from NCEP CFS Reanalysis and Reforecast (CFSRR) Project (Saha et al. 2014), and the other set was produced using the Multi-ocean Analyses Ensemble (MAE) initialization method (Zhu et al. 2012a,b, 2013). We aim to: (1) demonstrate that the ASM predictability has different characteristics in different phases of the ENSO cycle; and (2) investigate possible physical mechanisms for the enhanced seasonal predictive skill of the ASM rainfall in the ENSO decaying years, focusing on the spatio-temporal evolution of the ASM response from the El Niño peak phase to its demise phase. Especially, we intend to confirm that the Asian monsoon rainfall is more predictable during the subsequent summer in the demise phase of ENSO than in the ENSO developing years. In addition, the comparison of the seasonal predictive skill of the ASM rainfall between the two hindcasts sets with different initialization methods enables us to further explore the possible impact of the MAE initialization on the seasonal prediction of the ASM rainfall variability associated with ENSO.

Section 2 describes the observational data, the model (CFSv2), and two sets of hindcast experiments in detail. In Sect. 3, we identify the most dominant modes of the predicted and observed ASM rainfall variability and their association with ENSO, and examine the seasonal predictive skill and predictability of the ASM rainfall. Possible mechanisms for the enhanced predictability of the ASM rainfall in the ENSO decaying years are discussed in Sect. 4. Composite analysis of the ASM rainfall anomalies for six El Niño events further confirms better prediction of the ASM rainfall

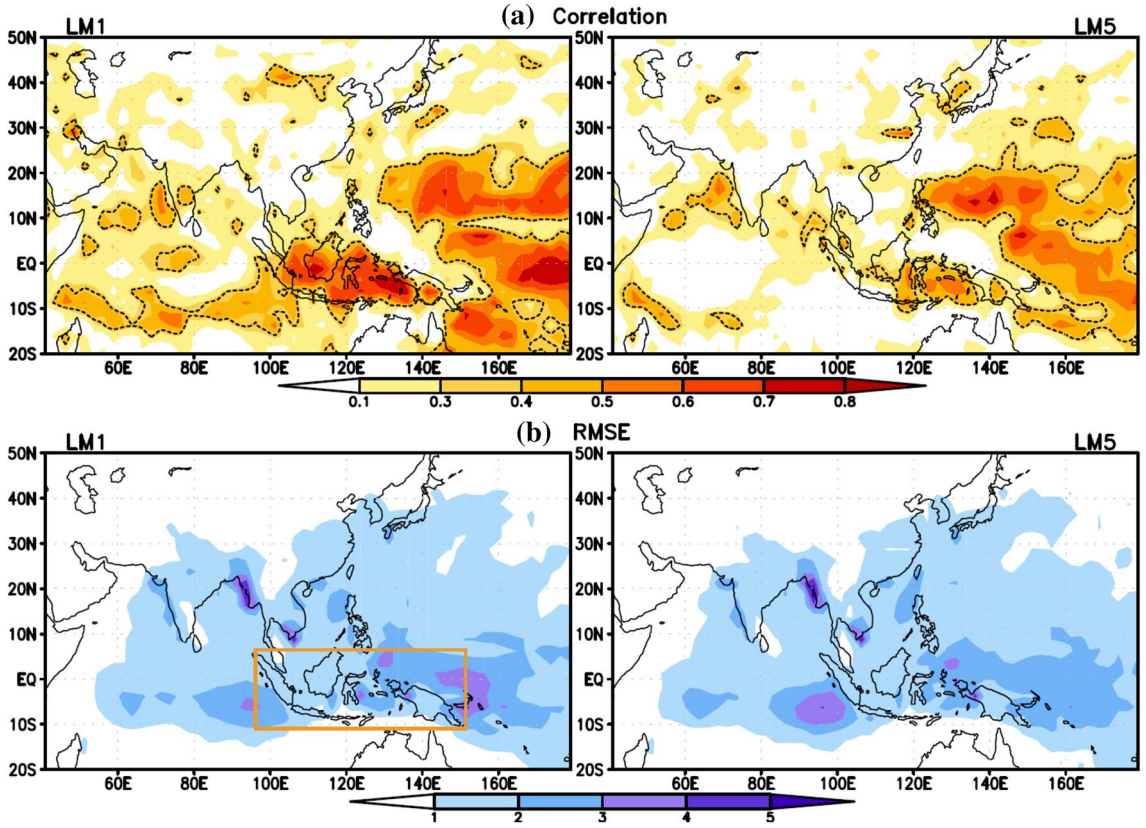

Fig. 1 **a** Temporal correlation coefficient skill and **b** RMSE (mm/day) of CFSv2 predicted JJAS (June–September) mean rainfall anomalies at 1-month lead (left) and 5-month lead (right) for 1979–2008. The dotted lines in **a** represent 95% confidence level, and the orange box in **b** indicates the domain of the Maritime Continent in this study

following ENSO at long leads than in the ENSO onset years in Sect. 5. Summary and discussion follow in Sect. 6.

2 Model and two independent seasonal hindcasts datasets

The CFSv2 is a coupled dynamical climate system. The atmospheric model of the CFSv2 is a lower resolution version of the Global Forecast System (GFS), which has a spectral horizontal resolution of T126 (equivalent to about 1° grid spacing) and 64 vertical levels in a hybrid sigma-pressure coordinate. The oceanic component is the Geophysical Fluid Dynamics Laboratory (GFDL) Modular Ocean Model (MOM) version 4. It has a horizontally 0.5° × 0.5° grid spacing in the poleward side of 30° with gradually increasing meridional resolution to 0.25° inside of 10° while there are vertically 40 levels (27 levels in the upper 400 m) with the maximum depth of about 4.5 km. The sea ice component is a 3-layer global interactive dynamical sea-ice model with predicted fractional ice cover and thickness (Winton 2000) while the land surface component is the Noah land surface model. The oceanic component is coupled between the atmosphere and sea ice at every 30 min by exchanging surface momentum, heat, freshwater fluxes, and sea surface temperature (SST). More details about CFSv2 can be found in Saha et al. (2014). The version of the model used in this study follows the revisions described in Huang et al. (2015).

Zhu et al. (2012a, b, 2013) demonstrated that poor representation of the uncertainty in Ocean Initial Conditions (OICs) is a major source of overconfidence in seasonal forecasts. Therefore, the forecasting reliability can be improved by better sampling the uncertainties in OICs through the MAE initialization approach. In this study, using the MAE initialization method for ocean ensemble generation, we have conducted CFSv2 hindcasts initialized with four different ocean analyses for 30 years (1979–2008): (1) NCEP Climate Forecast System Reanalysis (CFSR, Saha et al. 2010), (2) NCEP Global Ocean data Assimilation System (GODAS, Behringer 2007), (3) European Centre for Medium-Range Weather Forecast (ECMWF) COMBINE-NV (Balmaseda et al. 2010), and (4) ECMWF Ocean Reanalysis System 3 (ORA-S3, Balmaseda et al. 2008). Note that these ocean analyses are produced with their own respective ocean models, assimilation schemes and collections of observational datasets. For all four sets of CFSv2 hindcasts, the

instantaneous fields from the NCEP CFSR are commonly used as the atmosphere, land, and sea-ice initial conditions. Each set of hindcast experiments with the same OIC has four ensemble members by selecting atmospheric, land surface, and sea-ice states, which are the instantaneous fields at 00Z of the first four days in each starting month, respectively. Therefore, an ensemble of 16 members is generated for each hindcast. Unlike the instantaneous land and atmosphere initial conditions, monthly mean ocean fields are linearly interpolated to the start dates of each month, because the instantaneous oceanic fields are not always available for all four ocean analyses. For example, the average of January and February mean ocean fields is used as the OIC for the start days in February. As a result, it is possible that process of generating OICs may smooth out some characteristics of intraseasonal ocean variability, although it can in parallel reduce noise in the ocean analyses. Zhu et al. (2012b) have shown that the prediction skill of ENSO in the CFSv2 hindcasts initialized with the monthly mean OICs is comparable to that based on instantaneous OICs (see their supplemental materials). These hindcast experiments start every month from January to May and finish at the end of September each year from 1979 to 2008. Hence, the hindcasts starting in January include retrospective forecasts up to 9 months lead, ones starting in February include forecasts up to 8 months lead, and so on.

We have comprehensively evaluated the prediction skill and reliability of SST and precipitation in these hindcasts with the MAE initialization scheme (Shin et al. submitted). The CFSv2 hindcasts initialized with the different OICs differ substantially in their predictive skill as the lead-time increases. More importantly, there is no outstanding characteristic to determine which set of hindcasts performs the best or worst among the four different OICs. Rather, the best or worst performer varies in lead-month as well as starting calendar month. On the other hand, the prediction skill of the 16-member ensemble mean is equivalent to the best skill among the individual hindcasts for all lead times and all starting calendar months. This suggests that the forecast with the MAE initialization is more reliable than any of those derived from individual ocean analysis. In the remainder of this paper, we use the CFSv2 16-member ensemble mean hindcasts with the MAE initialization and refer them to as CFS_MAE.

In addition to CFS_MAE, we also analyzed the hindcasts from the NCEP CFSRR for 1982–2009, which were produced by NCEP using CFSv2 (Saha et al. 2014). The CFSRR hindcasts have instantaneous initial conditions from the NCEP CFS Reanalysis (CFSR, Saha et al. 2010) at 00Z, 06Z, 12Z, and 18Z for every 5 days beginning on January 1st of each year, with each run extending to 9 months. Therefore, their initial states are from a single reanalysis system and their ensemble members in both atmosphere and ocean initial states were generated by the lagged ensemble method, having an ensemble size of 24 forecasts for each month (see Appendix B of Saha et al. (2014) for details). In this study, we used 16-member hindcasts whose initial conditions (IC) are closest to the starting dates of CFS_MAE. For example, the 16 forecasts for May are from ICs on April 21 and 26, as well as May 1 and 6 at 00Z, 06Z, 12Z, and 18Z. The 16-member ensemble hindcasts starting from January to May are referred to as CFS_RR hereafter.

The observed monthly rainfall used for verification comes from the Climate Prediction Center (CPC) Merged Analysis of Precipitation (CMAP) data (Xie and Arkin 1997). The observed monthly SST data are the global the extended reconstructed SST, version 3 (ERSSTv3; Smith et al. 2008) and ocean surface heat fluxes are the objectively analyzed air-sea heat fluxes (OAFlux; Yu et al. 2008). The observed atmospheric fields are from the ERA-Interim atmospheric reanalysis. Boreal summer (June–September, JJAS) anomalies are calculated as the deviation of JJAS mean from the long-term climatology. Note that the climatology is separately defined for the periods of 1979–2008 for CFS_MAE and 1982–2009 for CFS_RR, in order to take advantage of full length of two hindcasts respectively. As expected, the observed anomalies of ASM rainfall from these two climatologies are nearly identical to each other (not shown).

The conventional empirical orthogonal function (EOF) analysis is used to identify the leading modes of the predicted and observed ASM rainfall anomalies respectively and investigate the seasonal predictive skill of each mode. To verify the robustness of the predicted patterns extracted by the EOF modes of the ensemble mean hindcasts, we also applied the maximized signal-to-noise EOF (MSN EOF) analysis to the ensemble ASM rainfall predictions. The MSN EOF is a statistical technique designed to maximize the ratio of the variance of the predictable signals to the variance of the unpredictable noise. The latter is estimated from the departures of individual members from their ensemble mean (Allen and Smith 1997; Venzke et al. 1999; Huang 2004; Liang et al. 2009). Since the unpredictable internal noise may be present in the ensemble mean if the ensemble size of the hindcasts is small (16 in our case), it may still affect the leading conventional EOF modes. On the other hand, the leading MSN EOF mode maximizes the signal-to-noise ratio and provides the temporal-spatial patterns of predictable signals, to be referred to as the most predictable pattern hereafter.

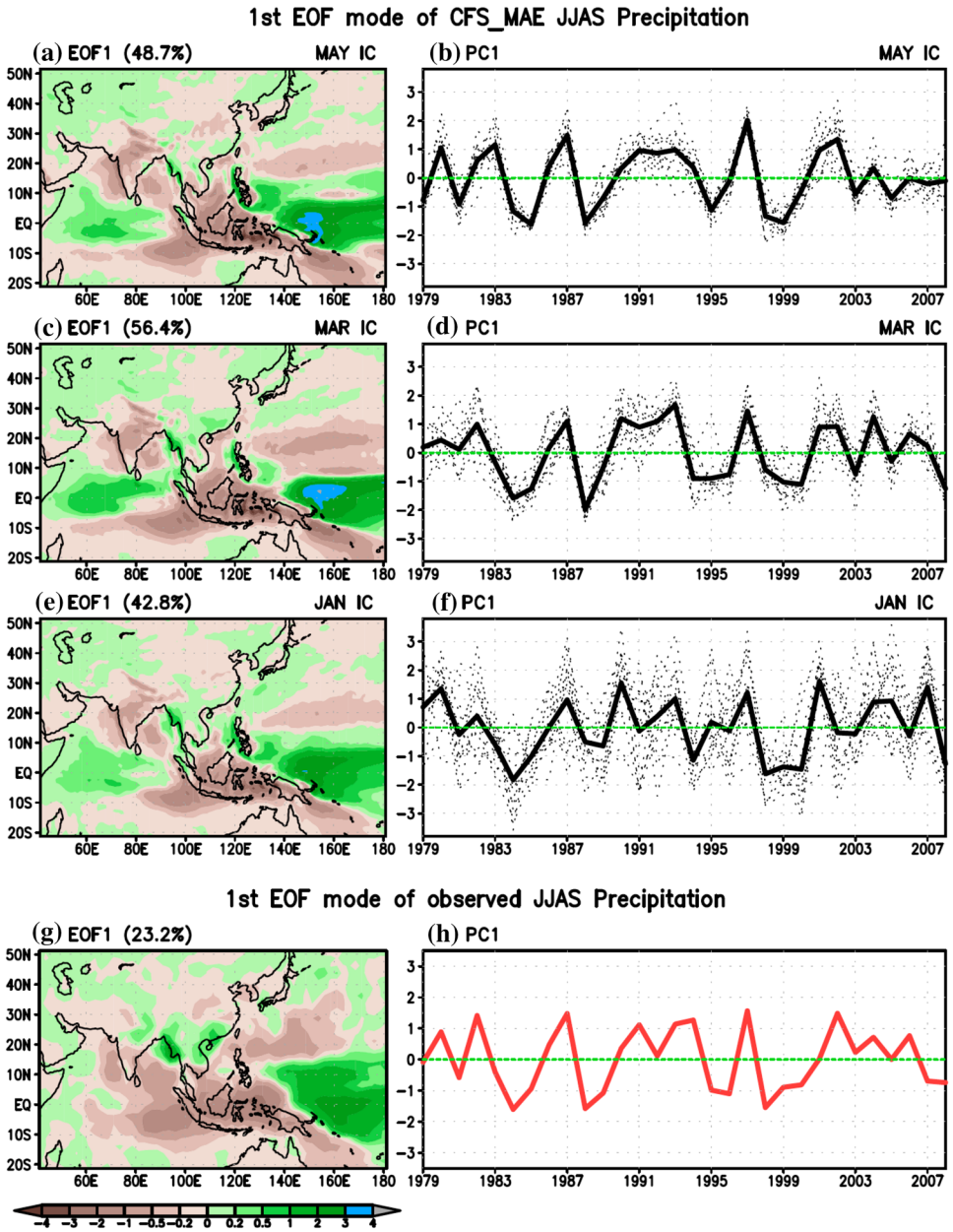

Fig. 2 **a** The first EOF mode (EOF1) of the CFS_MAE ensemble mean JJAS rainfall and **b** the corresponding normalized PC (solid black line) at 1-month lead (May IC). The dotted black curves in **b** represent the projected time series of CFS_MAE individual member forecast rainfall upon EOF1. **c, d** and **e, f** are the same as **a, b** but at 3-month lead (March IC) and 5-month lead (January IC), respectively. **g** EOF1 and **h** PC1 of the observed JJAS mean rainfall anomalies

3 Seasonal predictive skill and predictability of the most dominant ASM modes

Figure 2 displays the patterns of EOF1 and corresponding normalized principal components (PC1) time series of the predicted ASM anomalous rainfall in the CFS_MAE at 1-, 3-, and 5-month lead (i.e., starting in May, March, and January, respectively). This mode explains at least 42% of the total variance. Three branches of suppressed rainfall stretch out from a center over the Maritime Continent (MC)[1] into the South Pacific, the southern IO, and toward the Arabian Sea through the Bay of Bengal (BoB) and India. Below-normal rainfall is also evident over the northwest Pacific (NWP). In this study, the description of increased (or above-normal) or suppressed (or below-normal) rainfall in the EOF patterns refers to the periods when their corresponding PC time series are positive. On the other hand, increased rainfall is manifested over the tropical western Pacific, exhibiting a sharp contrast of wet and

[1] In this study, the MC is designated as the region of 10°S–10°N and 100°E–150°E (orange box in the left panel of Fig. 1b).

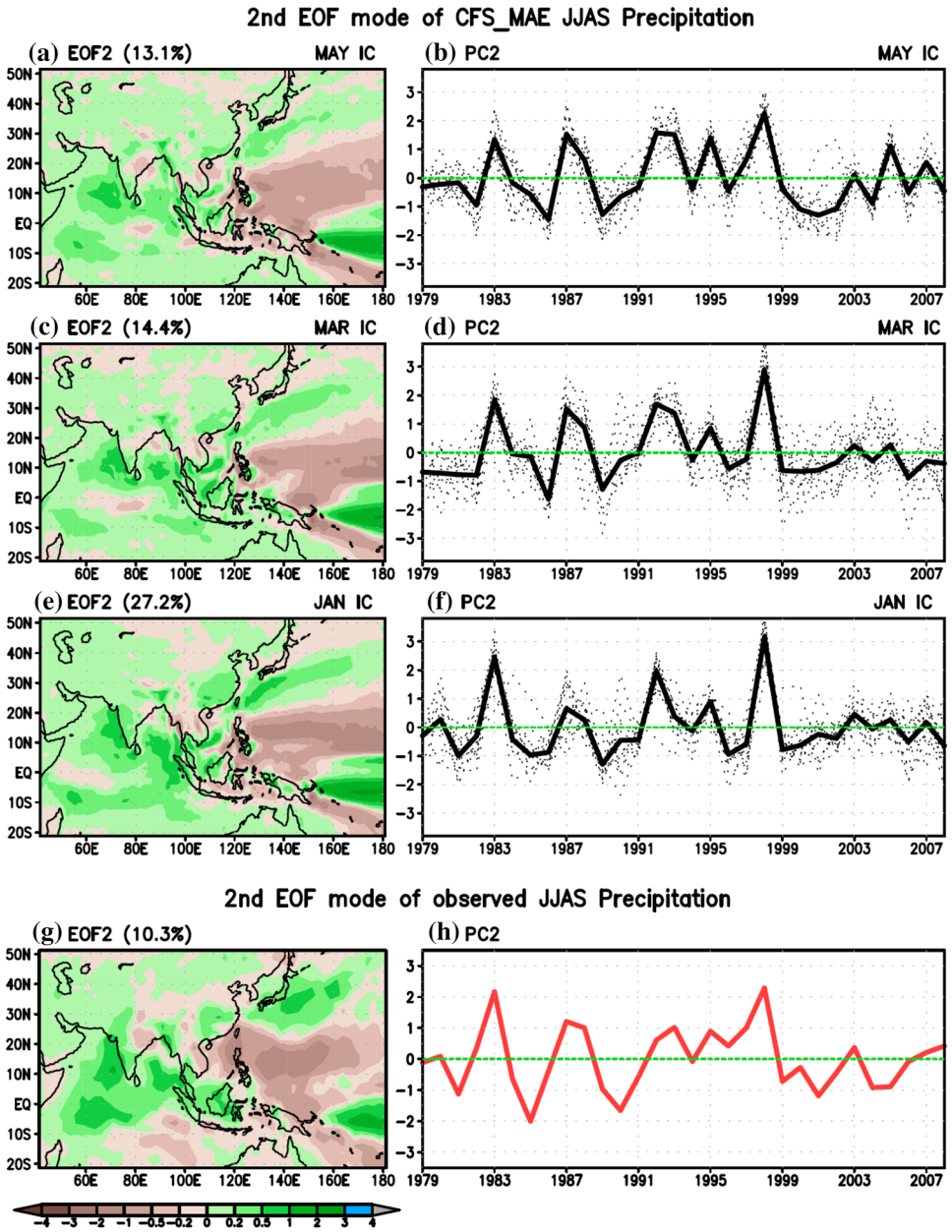

Fig. 3 Same as Fig. 2 but EOF2 and PC2

dry signals in the east–west direction. In EOF2 (Fig. 3), a key feature of its spatial pattern is that suppressed rainfall is centered over the NWP whereas above-normal rainfall is located to the north, and to the southwest from Indonesia and Malaysia to the Arabian Sea and tropical IO, and over the tropical western Pacific. The EOF2 of the CFS_MAE explains 13% of the total variance at 1-month lead and about 27% at 5-month lead. It is interesting that the variance of EOF1 (EOF2) continuously decreases (increases) from lead month 3–5. The EOF1 and EOF2 of the CFS_MAE at 4-month lead explain about 54 and 20% of the total variance, respectively. Overall, the spatial patterns of the two leading EOF modes do not change much as the lead-month increases.

The two leading EOF modes of the observed ASM rainfall variability for 1979–2008 are shown in Figs. 2g, h and 3g, h, which explain about 23.2 and 10.3% of the total variance, respectively. The observed ASM rainfall anomalies in this study are first de-trended before the EOF analysis is applied. The resulting second EOF mode in Fig. 3g is therefore more clearly distinguished from the third EOF mode (not shown), and the second PC (Fig. 3h) has no lower frequency signal than an interannual variation (i.e., no long-term trend), in contrast to a recent study of Wang et al. (2015) (their Fig. 2). In general, the two leading EOF patterns in observations are in good agreement with those of the predicted ASM anomalous rainfall in CFS_MAE, suggesting that CFS_MAE is capable of predicting the two

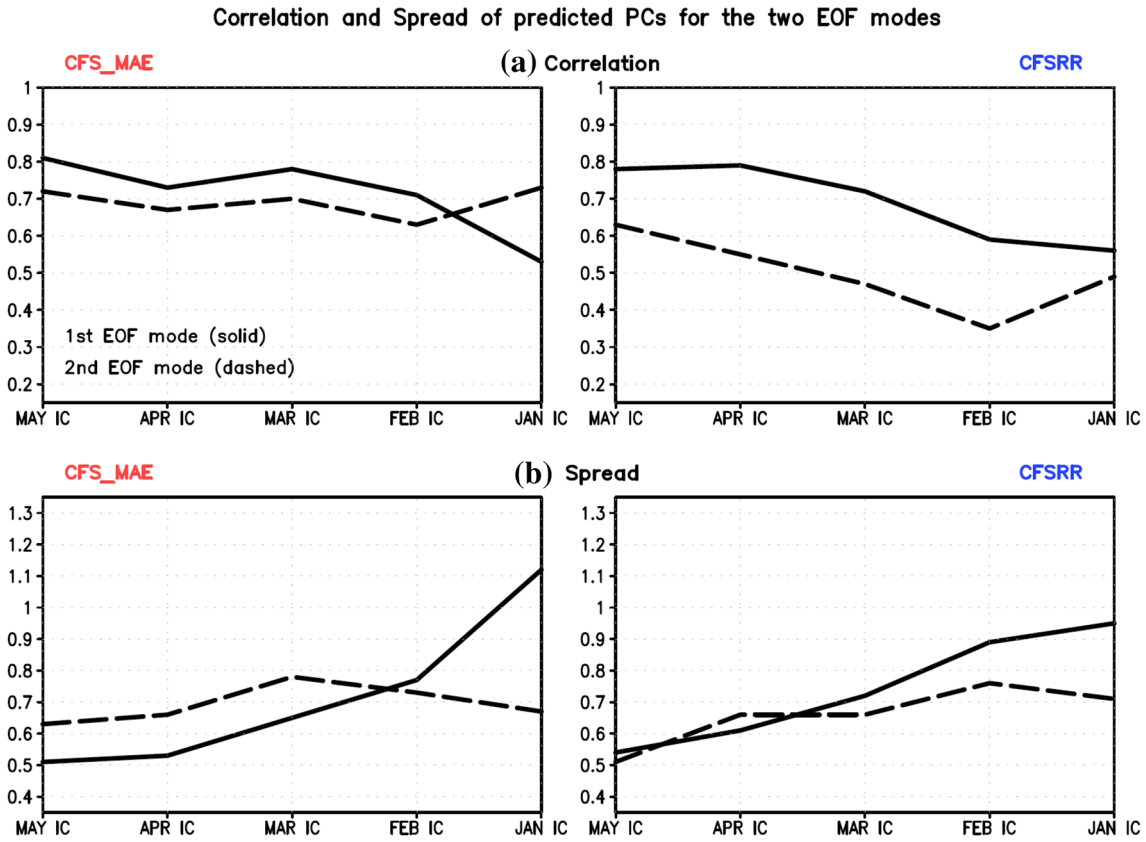

Fig. 4 **a** Correlation coefficients between the predicted and observed PC time series for the two EOF modes and **b** ensemble spreads of individual member PCs in (left) CFS_MAE and (right) CFS_RR. The solid and dashed curves represent the first and second EOF mode respectively. The abscissa is the starting calendar months from May to January, i.e., from1-month lead to 5-month lead

most dominant modes of the ASM rainfall interannual variability reasonably well in terms of the spatial pattern. In contrast, some discrepancies are also found. For example, above-normal rainfall over the western tropical IO in EOF1 (Fig. 2a, c, e) is stronger and broader than the observation (Fig. 2g). For EOF2, below-normal rainfall over the tropical southeast IO in the observations (Fig. 3g) is not well captured in the hindcasts at any lead month (Fig. 3a, c, e). In addition, the suppressed rainfall anomalies centered over the NWP extends northwestward to SCS and Taiwan, but are not well predicted in CFS_MAE, resulting in the southward shift of anomalous rainfall over Japan (Fig. 3a, c, e), compared with the observed anomalies (Fig. 3g).

For EOF1, the temporal correlation coefficient (TCC) between the ensemble mean predicted PC1 (thick black curves in Fig. 2b, d, f) and the observed PC1 (red curve in Fig. 2h) for 30 years is 0.81 at 1-month lead and then slowly decreases and finally drops from 0.71 at 4-month lead to 0.53 at 5-month lead (solid curve in the left panel of Fig. 4a). Conversely, the ensemble spread[2] of 16-member PCs (the projections of the ensemble members onto the ensemble mean EOF pattern, thin dotted curves in Fig. 2a, c, e) grows continuously as the lead-month increases (solid curve in the left panel of Fig. 4b). In particular, the ensemble spread at 5-month lead is more than twice the spread at 1-month lead. On the other hand, the TCC between the observed and predicted PCs in EOF2 is slightly smaller for lead months 1–4 than that of EOF1, with the maximum correlation difference (about 0.09) for May IC (1-month lead) (dashed curves in the left panel of Fig. 4a). However, the correlation at 5-month lead bounces back to 0.73, which is not only comparable to that of the 1-month lead forecast but also much higher (by about 0.2) than that of EOF1 at the same 5-month lead. The ensemble spread of 16-member PCs (thin dotted curves in Fig. 3a, c, e) gradually increases from lead month 1–3, but begins to decrease from 3-month

[2] The ensemble spread is calculated as the time mean standard deviation of each individual member PC's deviation from the ensemble mean PC.

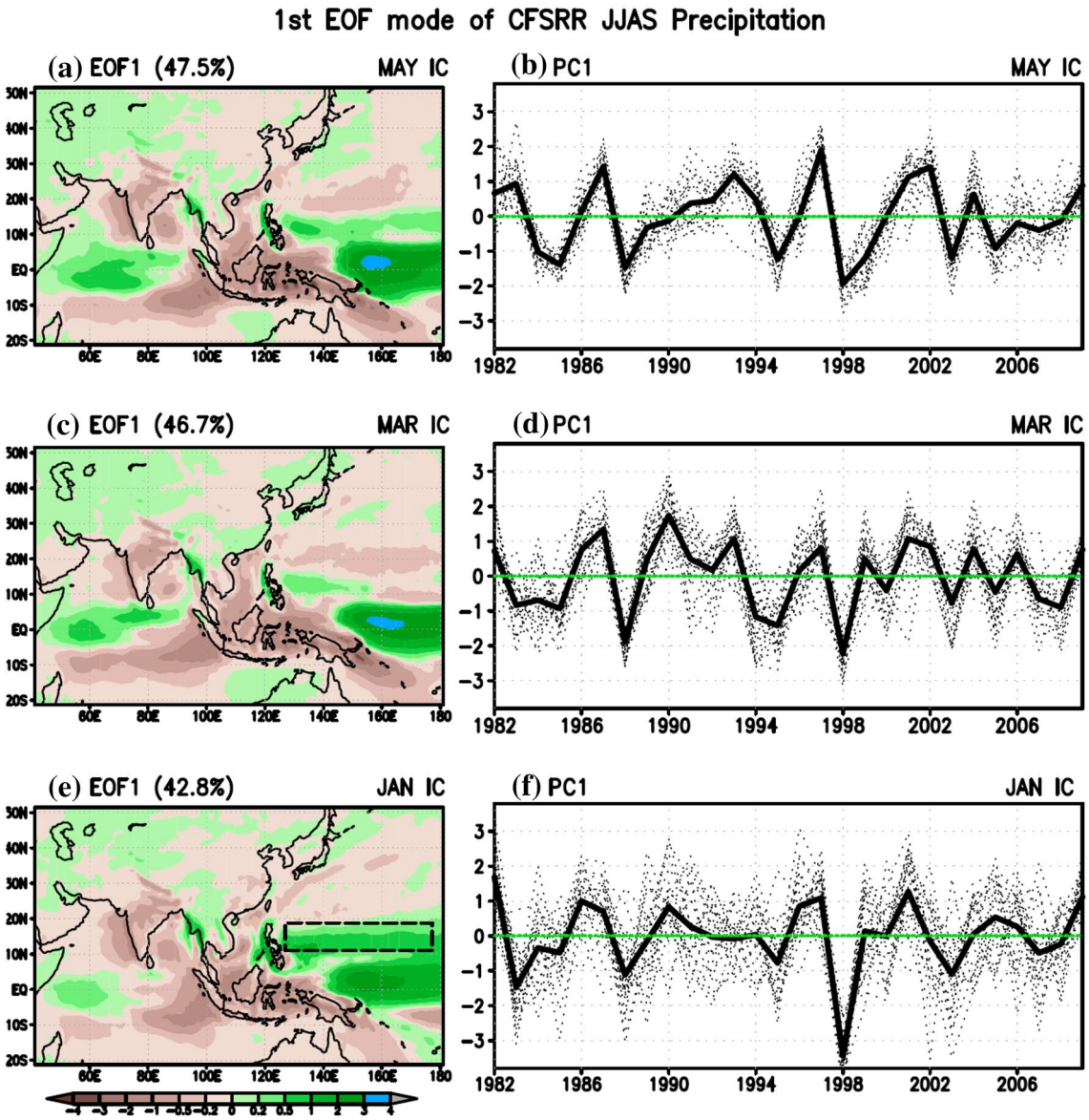

Fig. 5 Same as Fig. 2a–f except for CFS_RR (1982–2009)

lead and finally is only half as large as the spread for EOF1 at 5-month lead (dashed curves in the left panel of Fig. 4b).

As a result, we conclude that for EOF1, the CFS_MAE prediction of the ASM anomalous rainfall at long leads is less skillful with much larger ensemble spread than that at short leads; whereas the CFS_MAE long lead forecast (about two seasons ahead) can predict the ASM rainfall anomalies associated with EOF2 reasonably well, maintaining high correlation skill and small ensemble spread. This suggests the higher seasonal predictive skill of the ASM rainfall anomalies lies in EOF2 rather than EOF1.

The key features of the anomalous ASM rainfall spatial patterns in each mode of CFS_RR (Figs. 5, 6) are in general similar to those of CFS_MAE. However, the better prediction for EOF2 is not robust in CFS_RR (right panels of Fig. 4). For EOF1 in CFS_RR, the TCC between observed and predicted PCs gradually decreases from 1 to 5-month lead forecast, while the ensemble spread slowly increases (solid curves in the right panels of Fig. 4), consistent with the behavior of EOF1 in CFS_MAE (solid curves in the left panels of Fig. 4). For EOF2, on the other hand, CFS_RR does not maintain high correlation skill between observed and predicted PCs. Rather, the correlation skill degrades continuously from 0.63 (1-month lead) to 0.35 (4-month lead) (dashed curve in the right panel of Fig. 4a). The TCC is 0.49 at 5-month lead, resulting in the minimum difference of correlation skill between EOF1 and EOF2 at 5-month lead, but the prediction skill is overall much lower than that

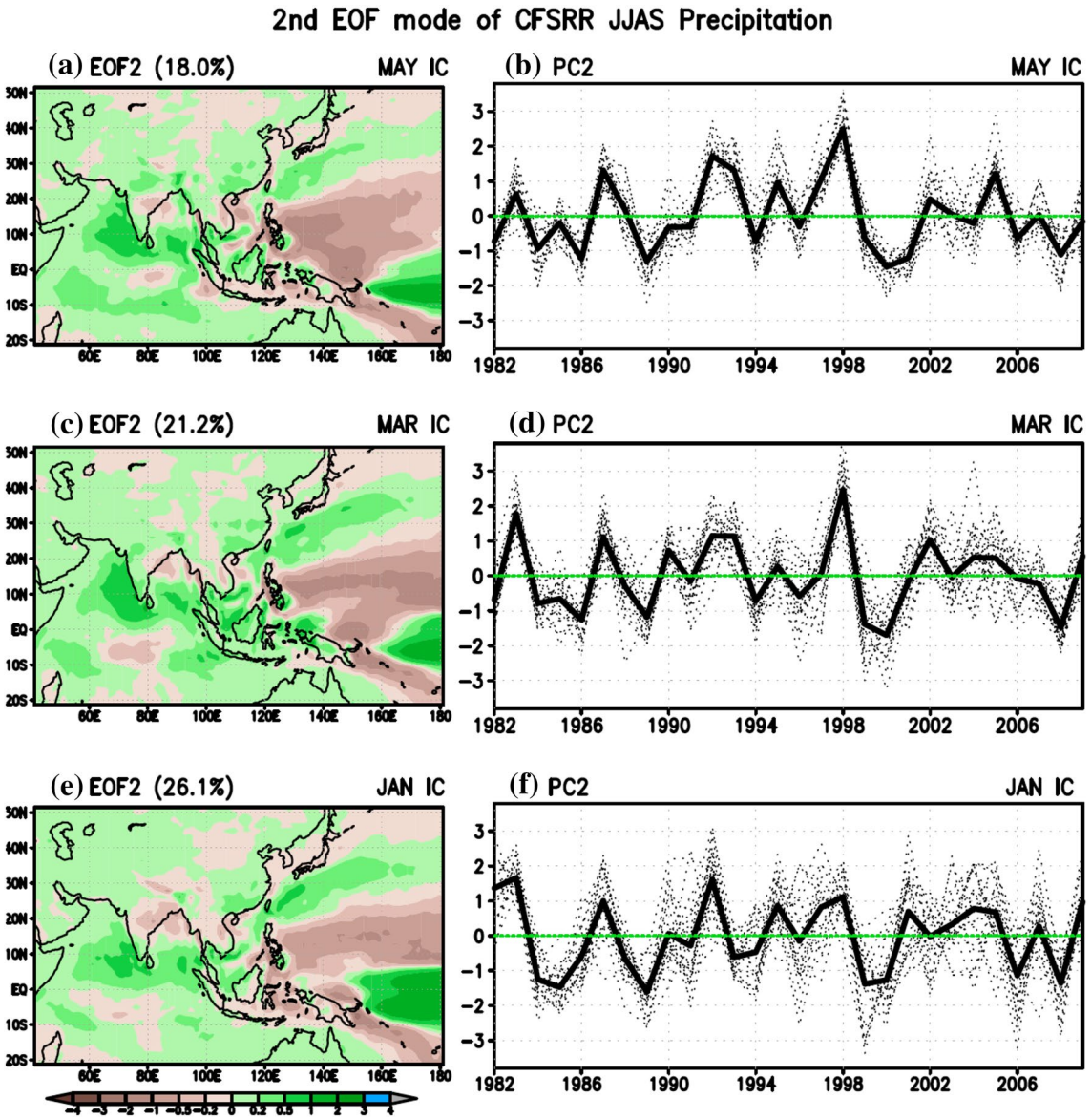

Fig. 6 Same as Fig. 3a–f except for CFS_RR (1982–2009)

of CFS_MAE. Besides, the ensemble spread of EOF2 in CFS_RR is also increasing as the lead-month increases, although it is smaller than that of EOF1 at long leads from 3-month lead (right panel of Fig. 4b). Consequently, the spread difference between EOF1 and EOF2 is not as large as that of CFS_MAE, especially at 5-month lead (Fig. 4b). The difference in the ASM prediction for EOF2 between CFS_MAE and CFS_RR will be further examined using the MSN EOF analysis.

Since ENSO plays a major role in modulating the ASM rainfall variability, it may be related to the two leading EOF modes. The temporal correlation coefficients are calculated between the observed monthly SSTA over the NINO-3.4 region and the observed PC time series of each mode for the same 30 years. The correlation coefficient for the first EOF mode (solid curve in Fig. 7) rapidly increases from March to June, slightly increases afterward, and finally reaches its maximum (about 0.89) in November and December. This indicates that the first EOF mode of the ASM rainfall anomaly is highly correlated with the tropical Pacific SSTA as the ENSO develops from boreal summer to boreal winter. In contrast, the correlation of NINO-3.4 and the second EOF mode (dashed curve in Fig. 7) peaks in January and drops in late spring and early summer, denoting the loss of its association with the tropical Pacific SSTA during the subsequent summer in the demise phase of ENSO, as will be described in the next section. Therefore, the two leading EOF modes of the ASM rainfall anomalies largely correspond to the ASM

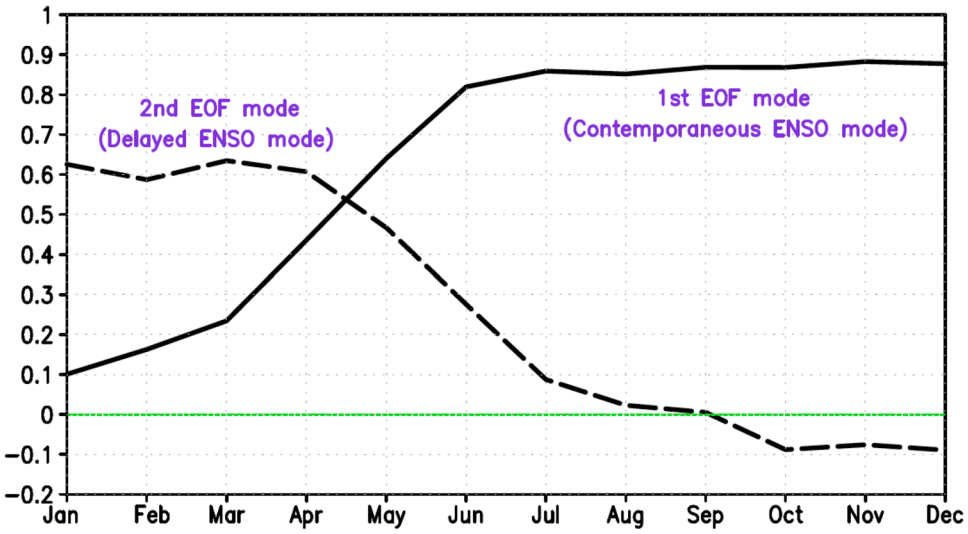

Fig. 7 The temporal correlation coefficients between the PC time series of each mode in Figs. 2h and 3h and monthly NINO-3.4 index for 1979–2008. Solid and dashed lines correspond to the first and second EOF mode, which are referred to as the contemporaneous and delayed ENSO mode, respectively

responses to the ENSO forcing in its developing and decaying years, and are then designated as contemporaneous and delayed ENSO modes, respectively in this study.

We investigate the most predictable patterns of the ASM rainfall variability in CFS_RR as well as CFS_MAE using the MSN EOF analysis to validate the two leading EOF modes derived by the conventional EOF analysis. It turns out that the most predictable mode (MSN EOF1) of CFS_MAE corresponds to the contemporaneous ENSO mode for May, April, and March ICs (from 1- to 3-month lead) while the delayed ENSO mode becomes the most predictable mode for February and January ICs (at longer leads) (Figs. S1 and S2). The MSN EOF1 and 2 of CFS_RR are also found to be similar to those of CFS_MAE (Figs. S3 and S4). Zuo et al. (2013) reported the same switch of the most predictable pattern of the ASM rainfall anomalies for the CFSv2 hindcasts at 5–8 month leads. Zhang et al. (2018) also indicated the most predictable patterns of low-level circulation in boreal summer over the tropical Indo-Pacific domain switched order from short to long leads. The switch in the order of the most predictable pattern may be associated with the starting month (i.e., whether a prediction starts before or after the spring barrier time) (e.g., Zhang et al. 2018). More importantly, the results from the MSN EOF analysis further substantiate the enhanced predictability of the delayed ENSO mode in both CFS_MAE and CFS_RR, with persistently high correlation skill and small ensemble spread as well as the most predictable mode at long leads (Fig. S5).

It is confirmed that like observation (Fig. 7), EOF1 (EOF2) of predicted ASM rainfall in CFS_MAE certainly corresponds to the contemporaneous (delayed) ENSO modes (Fig. S6a). While the correlation coefficient of EOF1 for CFS_MAE with January IC (solid blue curve of Fig. S6a) from summer to winter is much lower than those of EOF1 at shorter leads (solid red and green curves of Fig. S6a), it is interesting that the correlation coefficient of EOF2 from January to early summer is slightly higher as the lead-month increases (dashed colored curves of Fig. S6a). The relationship between each MSN EOF mode of CFS_MAE and the different ENSO phases is largely consistent with that of each conventional EOF mode (Fig. S6b), but note that the most predictable pattern switches from the contemporaneous ENSO mode to the delayed ENSO mode at long lead (blue curves of Fig. S6b).

If one closely compares the two ENSO modes of CFS_RR using between the conventional EOF and MSN EOF analysis, it may be recognized that one more west-east oriented branch of above-normal rainfall anomalies is located over the NWP (10°N–20°N) in the conventional EOF1 (represented by the dashed black box in Fig. 5e) with overly negative predicted PC, especially in the decay years of two strong El Niño events, 1983 and 1998 (Fig. 5f). However, it disappears in the MSN EOF1 contemporaneous ENSO mode with its PC closer to the observations, in particular at 5-month lead (Fig. S3e, f). On the other hand, compared with the conventional EOF2 (Fig. 6e, f), the suppressed rainfall anomalies over the same region are intensified with a larger amplitude predicted PC in 1983 and 1998 in the MSN EOF delayed ENSO mode (Fig. S4e, f) As a result, the contemporaneous and delayed ENSO modes in CFS_RR derived from the MSN EOF are more consistent with their counterparts in CFS_MAE as well as in observations. This may suggest that (1) the MSN EOF is a better tool to examine the predictive skill of seasonal forecasts, especially at long leads when the unpredictable internal noise is more intense; and (2) the multi-ocean analyses ensemble (MAE) initialization can help effectively reduce the internal noise growth in the seasonal forecasts of the ASM rainfall associated with ENSO, perhaps by minimizing the uncertainties in OICs. In addition to the different initialization strategies,

some specific features of the ocean reanalyses used to initialize the hindcasts may also have a secondary effect on the ASM predictive skill. For instance, the CFSR ocean analysis shows an unrealistic jump in the tropical SST around 1998/1999 (Xue et al. 2011), which leads to a warm bias there since 1999. The bigger influence of the CFSR bias in CFS_RR (e.g., Kumar et al. 2012; Xue et al. 2013; Shin and Huang 2017) may also be a factor resulting in its lower ASM predictive skill than that of CFS_MAE.

4 Possible mechanisms for the enhanced predictability of the delayed ENSO mode

Figures 8 and 9 show the observed and predicted ENSO-induced ocean and atmosphere anomalies from January to August, respectively. The former is regressed against the PC of the observed delayed ENSO (red curve in Fig. 3h) whereas the latter is regressed against the PC of the predicted delayed ENSO mode (EOF2) for CFS_MAE initialized in January (thick black curve in Fig. 3f). Since warm SST anomalies in the tropical central-eastern Pacific in January resemble the mature stage of El Niño and then continuously decline in time, they represent the temporal-spatial change of observed and predicted SST and atmospheric circulation response as an El Niño event evolves from its mature phase to its demise phase.

Over the NWP, anomalous anticyclonic low-level circulation (AAC) is apparent during the El Niño mature phase, with cold (warm) SST anomalies on the southeastern (northwestern) flank of the AAC (Fig. 8a, b). Although the associated SST anomalies become weaker in boreal summer, the NWP-ACC persists through August (Fig. 8). This is the key feature of observed ocean–atmosphere anomalies in the El Niño decay years (e.g., Wang et al. 2003; Xie et al. 2016). The persistent NWP–AAC is very well captured in CFS_MAE initialized in January (Fig. 9), but with much larger anomalies than in observations. Stronger and longer lasting El Niño events in the ensemble mean prediction of CFS_MAE may be responsible for the stronger response, as pointed out in previous studies (e.g., Wang et al. 2000, 2017).

Accompanied by a weakened Walker circulation, an AAC in the southeast IO forms and develops from boreal winter to spring, causing warming SST anomalies in the southwest IO in spring via ocean dynamics (Fig. 8a–d). Xie et al. (2016) discussed that the AAC in the southeast IO induces downwelling oceanic Rossby waves, and as they propagate westward, they deepen the thermocline in the southwest IO, giving rise to sea surface warming (Xie et al. 2002; Du et al. 2009). The resultant anomalous northerly wind crossing the Equator also contributes to relative SST warming (cooling) in the southern (northern) IO through the wind-evaporation-SST (WES) feedback (Xie and Philander 1994), leading to increasing (decreasing) rainfall anomalies in the southern (northern) IO in March and April, which in turn act to further enhance the anomalous northerly wind in May (Fig. 8c–e and left panels of Fig. 10a, b). This ocean–atmosphere interaction process over the tropical IO during the post-ENSO spring is also well reproduced in the hindcasts (CFS_MAE), displaying an asymmetrical pattern of anomalous SST, atmospheric low-level circulation, and precipitation between the northern and the southern portions of the IO (Fig. 9c–e and right panels of Fig. 10a, b).

When the ASM begins in May, anomalous easterly wind over the northern IO acts to reduce the mean southwesterly monsoon flow, resulting in increasing anomalous surface latent heat fluxes and therefore SST warming, while the northeasterly anomalies over the tropical NWP still increase the northeast trade mean flow, causing SST cooling there via the WES feedback (Wang et al. 2000) (Fig. 8e and left panel of Fig. 10c). The increased shortwave radiative effect due to suppressed rainfall over the northern IO also contributes to the northern IO SST warming (not shown). As a result, an inter-basin dipole structure of SST anomalies is evident in May, with the tropical IO warming and tropical NWP cooling (Fig. 8e). The CFS_MAE accurately predicts these WES feedback processes, the resulting inter-basin SST dipole pattern, and the anomalous precipitation patterns, in particular, over the Indo-NWP region (Figs. 9e, 10c).

In the subsequent summer, the enhanced SST warming over the northern IO and SCS and persistent NWP–AAC are apparent in both the observations and the predictions (Figs. 8f–h, 9f–h), and the spatial pattern of the predicted rainfall anomalies and their month-to-month evolution is also largely in good agreement with the observed (Fig. 11). One apparent disagreement between the observations and predictions is the location of the NWP–ACC center in June (Fig. 8f vs. Fig. 9f, and black contours in Fig. 11a), probably associated with the delayed demise of the predicted El Niño event with its stronger intensity. This causes the southward shift of southwest-northeast oriented East Asia summer monsoon in the prediction (green shading in Fig. 11a, b), which is commonly shown in the delayed ENSO mode of both CFS_MAE (Figs. 3 and S2) and CFS_RR (Figs. 6 and S4). The insufficient northwestward expansion of the NWP subtropical high in the CFSv2 during boreal summer is also documented in Shin and Huang (2016).

The enhanced northern IO warming in late spring/early summer in turn activates eastward propagating atmospheric Kelvin waves, playing a role in the maintenance and/or enhancement of the NWP-AAC (Xie et al. 2009, 2016). This so-called capacitor effect in the IO is evident in observations and is also reasonably captured in the predictions, except for the NWP-AAC in September, which survives in the predictions, in contrast to the

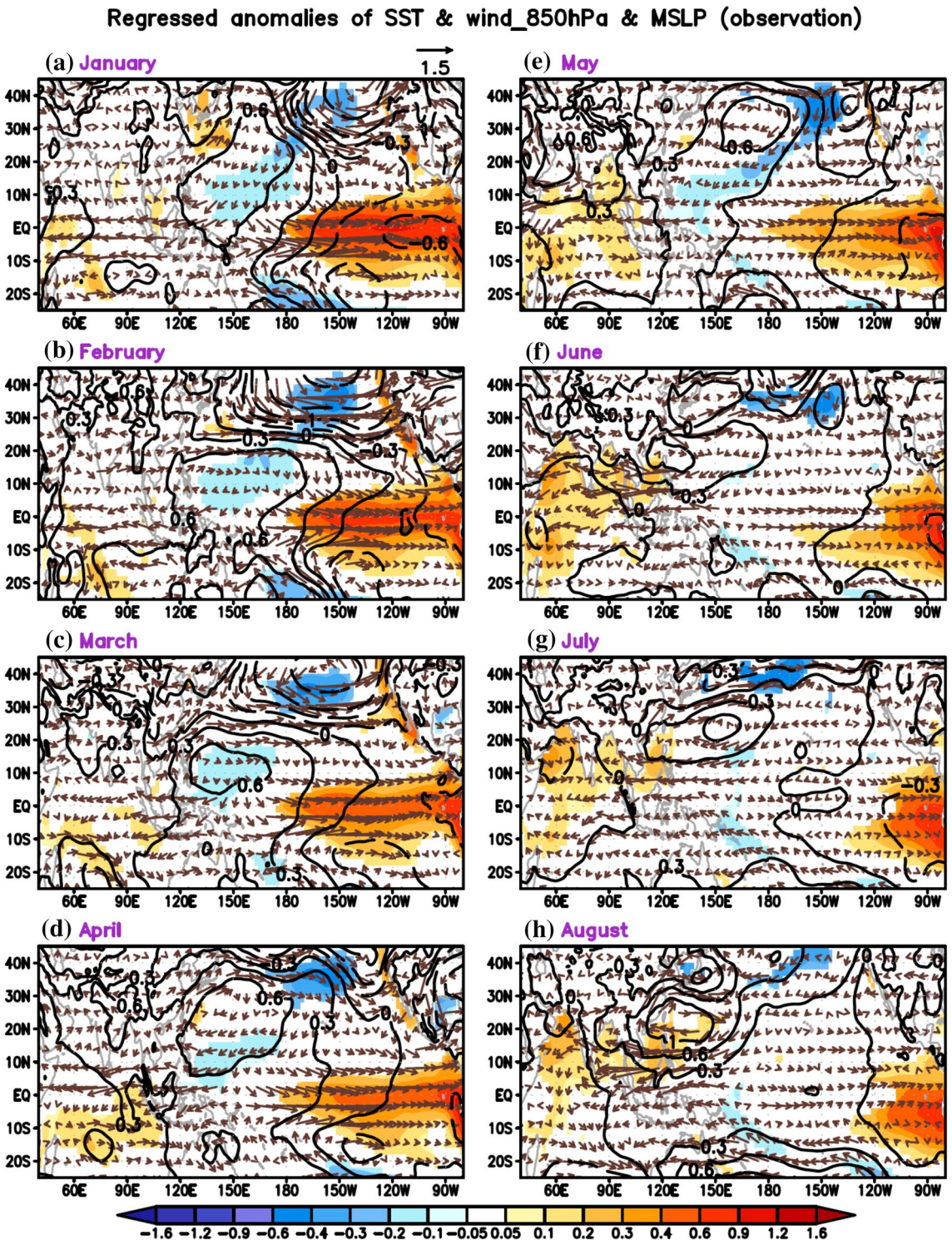

Fig. 8 Observed anomalies of SST (shaded at the 90% confidence level, °C), wind at 850 hPa (vectors, m/s), and mean sea level pressure (SLP) (contours, hPa) regressed against the delayed ENSO mode's PC of the observed ASM rainfall anomalies in Fig. 3h. The shading scale for the SST anomalies is shown at the bottom. The contours are ±0.3, ±0.6, ±1, ±2, and ±4 hPa. The SST is from the global monthly extended reconstructed SST, version 3 (ERSSTv3) while the mean SLP and wind at 850 hPa are from the ERA-Interim atmospheric reanalysis

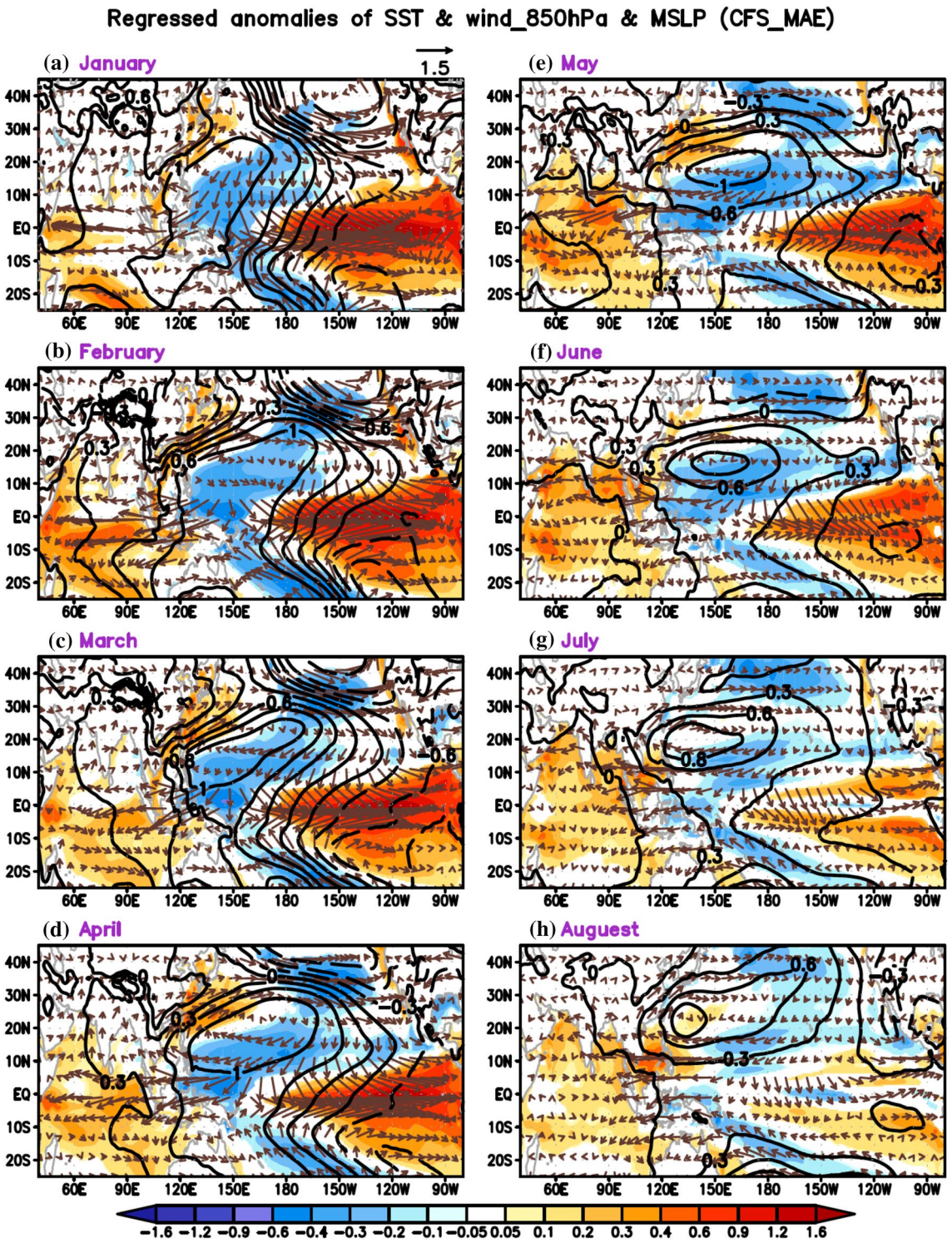

Fig. 9 Predicted anomalies of SST (shaded at the 90% confidence level, °C), wind at 850 hPa (vectors, m/s), and mean SLP (contours, hPa) regressed against the delayed ENSO mode's PC of CFS_MAE at 5-month lead (January IC) (Fig. 3f). The shading scale for the SST anomalies is shown at the bottom. The contours are ±0.3, ±0.6, ±1, ±2, and ±4 hPa, but one more contour with +0.8 is also added in (f–h). The SST, wind at 850 hPa, and mean SLP are from the ensemble mean forecasts of CFS_MAE at 5-month lead (January IC)

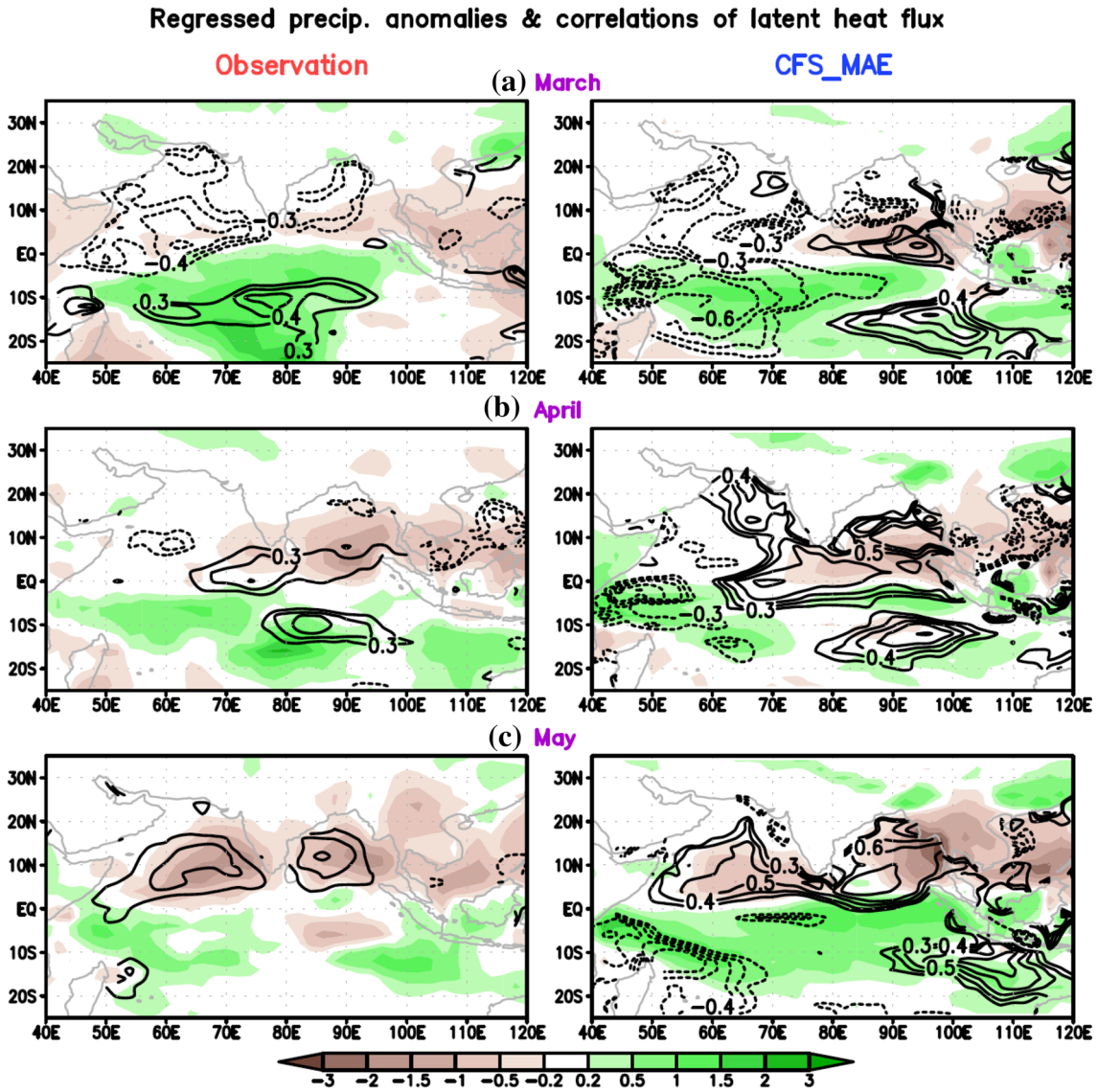

Fig. 10 Regressed anomalies of precipitation (shaded, mm/day) and correlations of ocean surface latent heat flux anomalies (positive contours imply more evaporation from the surface) with respect to the delayed ENSO mode's PC of (left) the observed ASM rainfall anomalies in Fig. 3h and (right) the predicted ASM rainfall anomalies in CFS_MAE at 5-month lead in Fig. 3f. The ocean surface latent heat fluxes are from Objectively Analyzed air-sea heat Fluxes (OAFlux). The shading scale for the rainfall anomalies is shown at the bottom. The contours are ±0.3, ±0.4, ±0.5, ±0.6, ±0.7, ±0.8 and ±0.9 (over the 90% confidence level)

observations (Fig. 11). Another possible mechanism for the persistent NWP-AAC through the post-ENSO summer is the local air-sea coupling (the WES feedback) over the NWP (Wang et al. 2003; Xiang et al. 2013). SST cooling on the southeast flank of the NWP-AAC lasts longer with much stronger intensity in the predictions (Fig. 9f–h) than the observations (Fig. 8f–h), which may partially account for the long-lasting NWP-AAC in September in CFS_MAE (Fig. 11).

5 Prediction of the ASM rainfall anomaly preceding/following El Niño events

In addition to the sophisticated statistical methods (the conventional EOF and MSN EOF analyses), we examine how well the model predicts the ASM rainfall anomalies in the onset and decay years of the El Niño events. For the 1997–1998 El Niño, the strongest El Niño event in

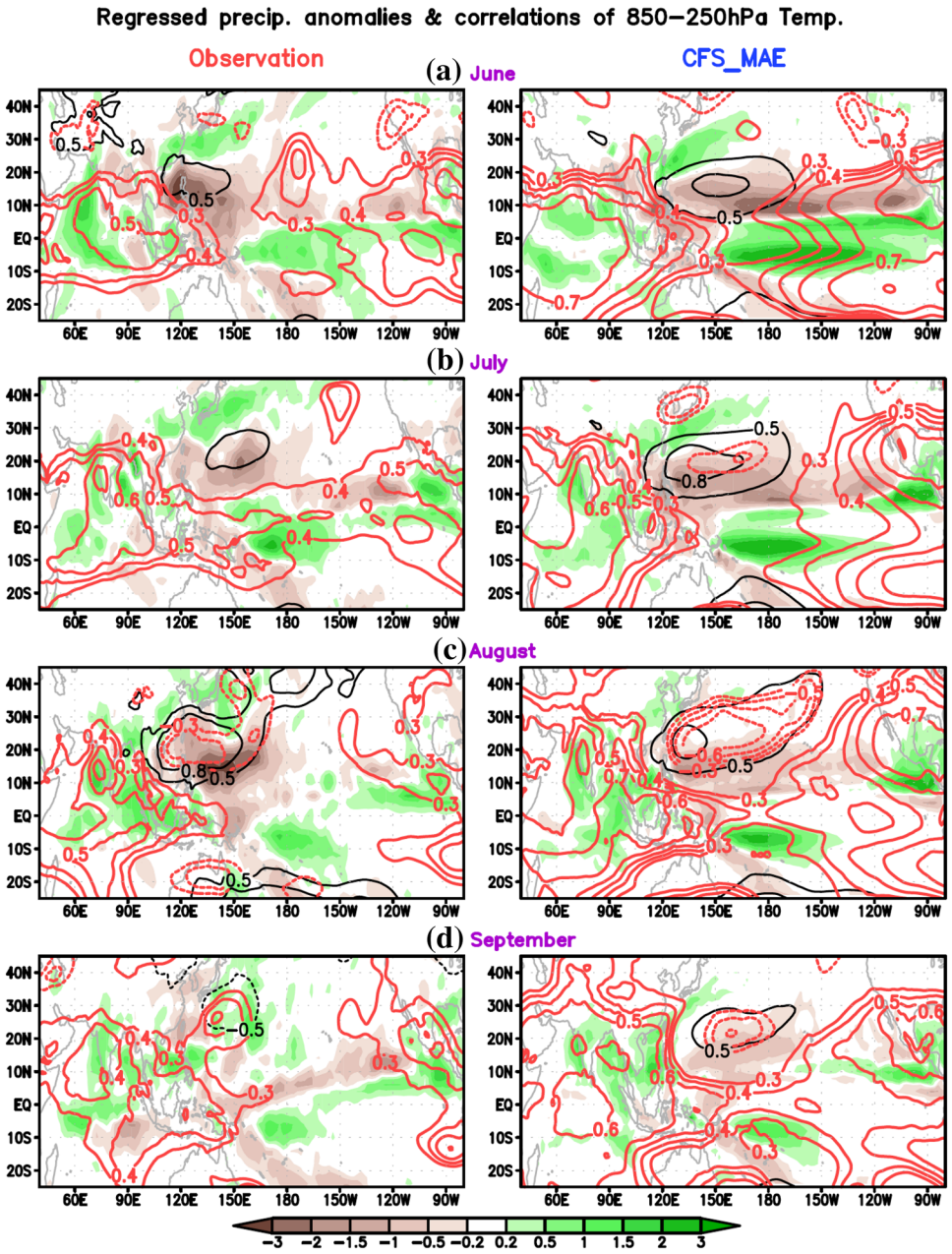

Fig. 11 Regressed anomalies of precipitation (shaded, mm/day) and correlations of tropospheric temperature averaged between 850 and 250 hPa (red contours) with respect to the delayed ENSO mode's PC of (left) the observed ASM rainfall anomalies in Fig. 3h and (right) the predicted ASM rainfall anomalies in CFS_MAE at 5-month lead in Fig. 3f. The solid (dashed) black contours indicate the center of anomalous surface anticyclonic (cyclonic) circulation (i.e., regressed mean SLP anomalies w.r.t. the delayed ENSO mode's PCs). The shading scale for the rainfall anomalies is shown at the bottom. The contours are ±0.3, ±0.4, ±0.5, ±0.6, ±0.7, ±0.8 and ±0.9 (over the 90% confidence level)

this period (1979–2008), the model predicted the ASM seasonal rainfall anomalies much better in its decay year (1998) than the onset year (1997) (Fig. 12). In 1997, for example, the observed enhanced rainfall anomalies over the region from northeastern India to southern China as well as over the tropical northern IO are not captured in the CFS_MAE prediction, resulting in an overestimated drought in all of India (Fig. 12a, c). In the tropical western Pacific, the increase of anomalous rainfall in CSF_MAE is also shifted to the west, compared with that of the observed. In contrast, the 5-month lead forecast in 1998 agrees well with the observed ASM rainfall anomalies and the model prediction also captures the IO dipole structure reasonably well (Fig. 12b, d).

It should be pointed out that the model forecast is consistent with the canonical ENSO-monsoon relationship. The observed situation in 1997 is unique in that a strong Indian dipole SST pattern quickly developed during the summer season (e.g., Webster et al. 1999), which

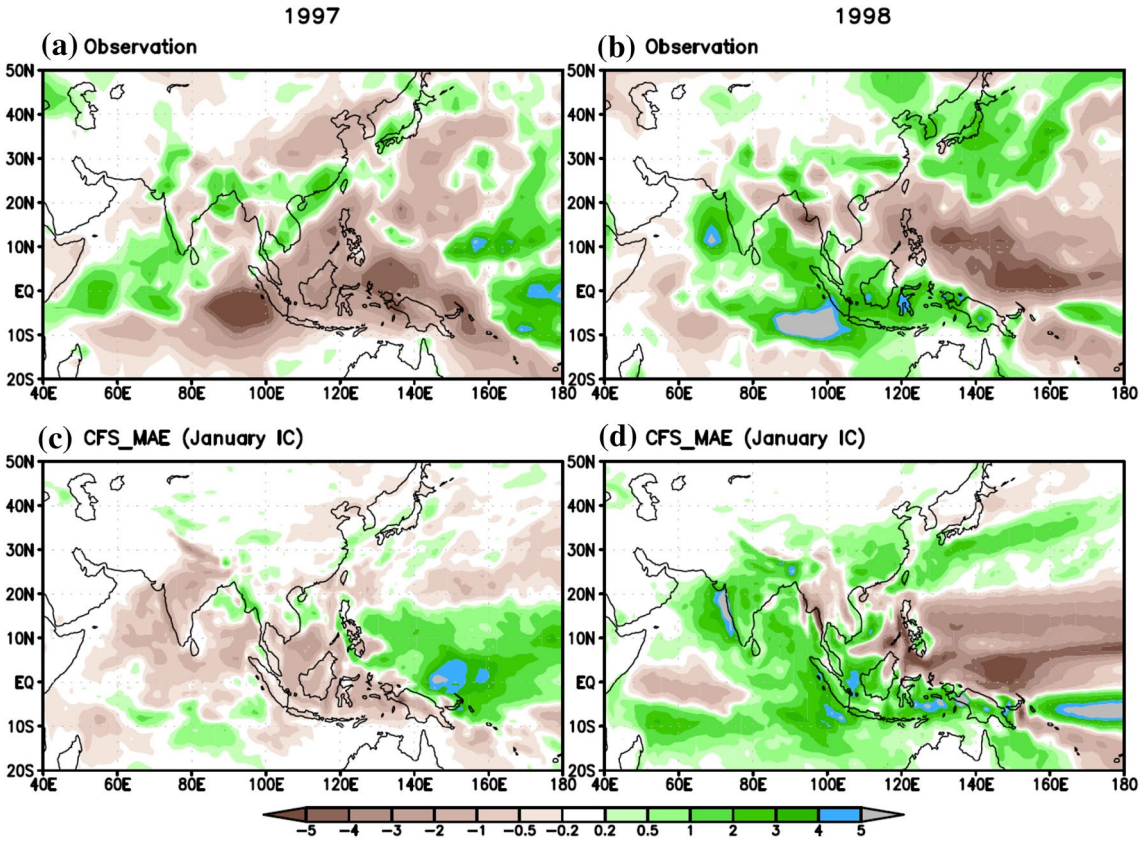

Fig. 12 Observed JJAS rainfall anomalies in **a** 1997 and **b** 1998, the onset and decay year of 1997–1998 El Niño, and **c** and **d** are same as **a** and **b** but for the CFS_MAE predicted JJAS rainfall anomalies at 5-month lead (January IC)

may have eased the anticipated drought conditions (e.g., Achuthavarier et al. 2012). Therefore, one may want to see the seasonal prediction of the anomalous ASM rainfall for more El Niño events. Figure 13 shows observed and predicted composite anomalies of the ASM rainfall for all El Niño events occurring during the period in the onset (decay) years in the left (right) panels. The six events over 30 years (1979–2008) include 1982–1983, 1991–1992, 1994–1995, 1997–1998, 2002–2003, and 2006–2007 El Niño events.[3] In the onset years, most of Asia experienced anomalously dry summers except for southern China, Vietnam, and Myanmar, while enhanced rainfall occurred in the tropical western Pacific (Fig. 13a), indicating a sharp contrast of anomalous rainfall in the east-west direction, with below (above) normal rainfall in the MC and the southeastern IO (tropical western Pacific) as seen in the first EOF mode (Fig. 2g). In general, this key characteristic of the observed ASM anomalies in the onset years is reasonably predicted in the CFS_MAE initialized in May and March (Fig. 13c, e), but not well predicted in the January IC hindcasts with weak above-normal anomalous rainfall in the MC and the southeastern IO (Fig. 13g) in contrast to the observed. As the lead-month increases, the decreasing amplitude of the composite predicted rainfall anomalies may imply that the predicted ASM rainfall anomalies in the developing El Niño years are quite different from event to event with large uncertainty, and therefore they presumably cancel each other out. To validate this speculation, we calculated the leading EOF modes of predicted ASM rainfall departures of individual members from their ensemble mean (i.e., noise EOF modes) in CFS_MAE initialized in January. The spatial pattern of the first leading noise EOF mode (not shown) bears some resemblance that of the second leading MSN EOF (Fig. S1e), consistent with the divergent growth of the predicted contemporaneous ENSO mode at long leads.

On the other hand, the pattern of observed anomalous rainfall during the summer of the El Niño decay years seems largely opposite to that of the onset years. In decay years, enhanced rainfall is aligned from northwest to southeast from the Arabian Sea to the MC via India and the BoB, and also in the tropical IO, whereas reduced rainfall centered in

[3] Note that two, back-to-back El Niño events in 1986–1988 are excluded.

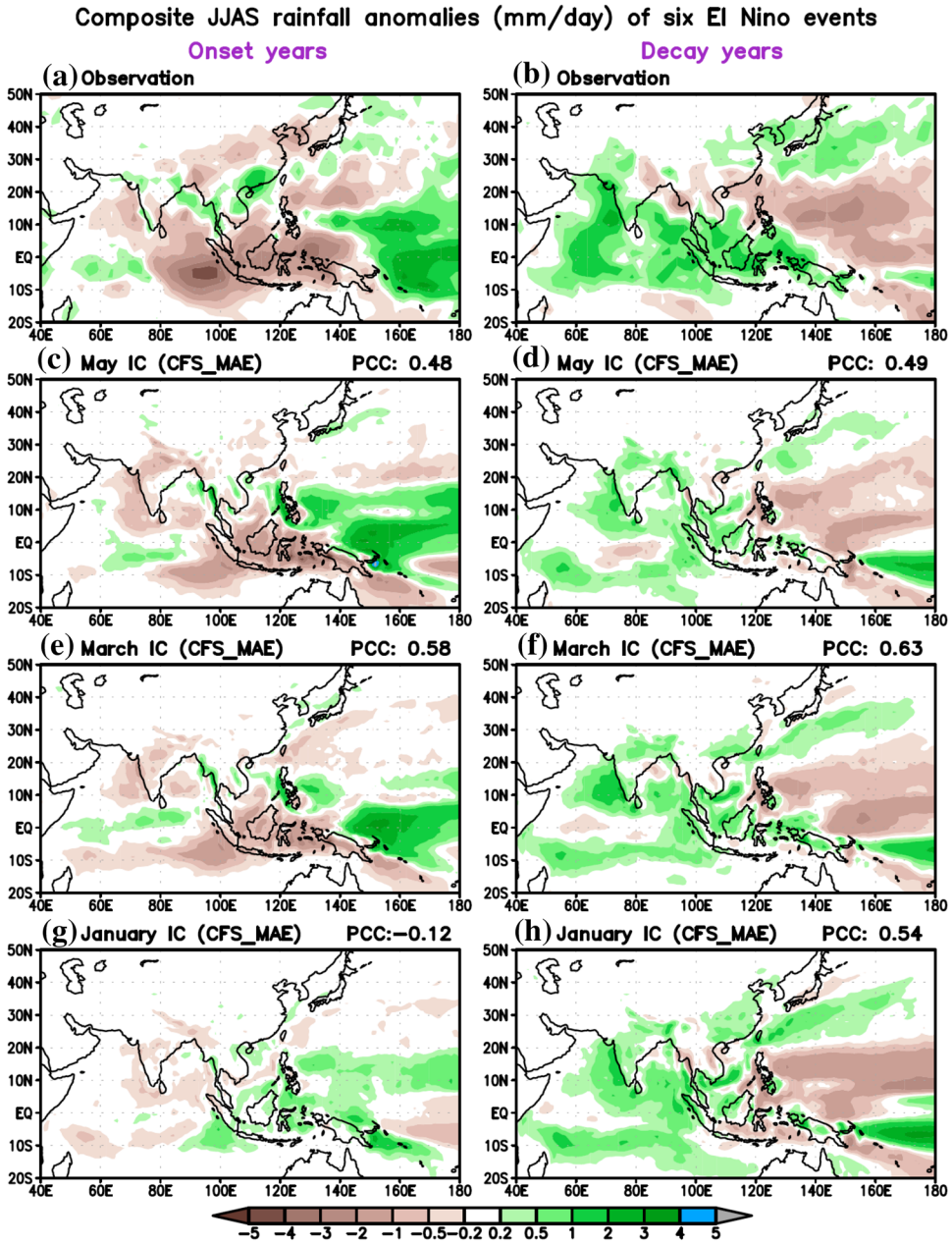

Fig. 13 Composite JJAS mean rainfall anomalies in the onset and decay years of six El Niño events in observation (**a, b**) and in CFS_MAE at (**c, d**) 1-month lead, **e, f** 3-month lead, and **g, h** 5-month lead. Numbers at the right top of each panel (**c**–**h**) denote the pattern correlation coefficients (PCC) of the rainfall anomalies between observation and predictions

the subtropical NWP stretches northwestward to the western China and the northeastern India (Fig. 13b). The latter is sandwiched by another band of above-normal rainfall from the Yangtze River in China to Korea and Japan. The spatial anomalous rainfall pattern in the El Niño decay years is very similar to that of the second EOF mode in Fig. 3g. For all three initial months, the predicted ASM rainfall anomalies of CFS_MAE in the decay years are in good agreement with the observed ones, with the enhanced (reduced) rainfall over the IO, BoB, Arabian Sea, and India (in the subtropical NWP) (Fig. 13d, f, h). The pattern and magnitude of the predicted composite rainfall anomalies are quite independent on lead-time. As a result, the spatial pattern correlation coefficients (PCC) between the observed and the predicted ASM rainfall anomalies in the El Niño decay years are greater than that in their onset years, in particular, at longer leads. In fact, the PCC for January IC in the decay years is comparable with those at shorter leads, in contrast to a noticeable drop of the PCC for January IC in the onset years.

6 Summary and discussion

Using two independent sets of CFSv2 seasonal hindcasts (CFS_MAE and CFS_RR), the seasonal predictive skill of the ASM rainfall variability is investigated, with an

emphasis on its dominant modes. A comparison of the ASM rainfall prediction between the two sets of hindcasts with different initialization methods enables us to further explore the possible impact of the MAE initialization on the seasonal prediction. Statistically, the two leading (conventional) EOF modes of the observed ASM rainfall anomalies largely correspond to the ASM responses to the ENSO events in their developing and decaying years, and so are designated as the contemporaneous and delayed ENSO responses, respectively. The corresponding EOF modes from both seasonal hindcasts at different leads largely reproduce the spatial patterns of the observations. In general, the CFS_MAE predicts these two dominant ASM modes reasonably well up to a lead-time of 5 months. More importantly, the predictive skill of the ASM rainfall about two seasons ahead is much higher in the case of the delayed ENSO mode than in the contemporaneous one. The predicted PC time series of the delayed ENSO mode maintains high correlation skill and small ensemble spread as the lead-time increases, whereas the skill of forecasts of the contemporaneous ENSO mode is significantly degraded in both measures after one season. These results imply higher ASM predictability in the aftermath of ENSO events. Analysis of the strongest El Niño event (1997–1998) during the period of this study and composite analysis of the ASM anomalous rainfall for six El Niño events further confirm that the ASM rainfall is more predictable following El Niño, especially when the CFSv2 hindcasts are initialized in boreal winter.

It is interesting to note that when the conventional EOF analysis is applied to the ensemble mean ASM rainfall anomalies from the CFS_RR hindcasts, the delayed ASM response to the tropical forcing (ENSO) does not seem to be clearly distinguished from the contemporaneous ENSO mode, especially in the hindcasts initialized in boreal winter. As a result, the enhanced seasonal predictive skill of the delayed ASM response to ENSO is not obvious in CFS_RR. This discrepancy seems to be associated with the stronger influence of the unpredictable internal noise in the system. In fact, the results from an MSN EOF analysis for CFS_RR, which maximizes the signal-to-noise ratio of the leading EOF modes, conform more with the CFS_MAE results in demonstrating the enhanced predictability of the delayed ENSO mode at about two seasons lead, with persistently high correlation skill and small ensemble spread. In fact, the delayed ENSO response at long leads becomes the most predictable pattern with smaller ensemble spread than at short leads while the contemporaneous ENSO response becomes the second most predictable pattern as the ensemble spread continuously increases with the lead month. On the other hand, the leading MSN EOF modes derived from the CFS_MAE hindcasts are very consistent with the conventional EOF analysis. Consequently, we conclude that the MSN EOF is a better tool to examine the predictability of seasonal forecasts, especially at long leads when the unpredictable internal noise plays a bigger role.

It is not clear why the CFS_RR hindcasts seem to show higher internal noise influence than that in CFS_MAE with respect to the ASM rainfall predictions. One possible reason is the lagged ensemble approach of generating ensemble means using ensemble members with initial dates spanning nearly a month for CFS_RR (Saha et al. 2014). Furthermore, despite that CFS_MAE has the same ensemble members as CFS_RR, the consistent results from both the conventional EOF and the MSN EOF in CFS_MAE may imply that better sampling of uncertainties in OICs (via the MAE initialization) can effectively diminish the effect of the unpredictable internal noise in the seasonal forecasts of the ASM rainfall anomalies associated with ENSO. This also suggests that better initial conditions including new ensemble techniques may be critical to improving the seasonal predictive skill in the current generation coupled climate models. Further investigation is needed to fully evaluate this speculation.

By analyzing real-time forecasts of NINO-3.4 index in 2002–2016 (including both dynamical and statistical models), Zheng et al. (2016) demonstrated that ENSO decay phase is more predictable than its development phase. Therefore, the predictive skill differences of ASM rainfall between ENSO decay and development phases may partly be attributed to the predictive skill differences of ENSO between its development and decay phases. Furthermore, the improved ASM predictive skill during the ENSO decaying phase is also associated with the regional air-sea feedbacks in the Indo-Pacific region, which are intensified from ENSO maturing to decaying phases and enhance the seasonal ASM predictability in these episodes. The delayed impact of ENSO on atmospheric circulation and SST in the Asian monsoon region is characterized by the evolution of the warm SST anomalies in the tropical IO and SCS during the spring of the ENSO mature phase and the persistence of the anomalous high surface pressure in the western Pacific through the subsequent summer. It is demonstrated that the CFS_MAE initialized in boreal winter is surprisingly good at capturing the spatio-temporal evolution of inter-basin ocean–atmosphere interactions between the tropical IO and the NWP from the ENSO peak to the ENSO demise phase. It accounts for the enhanced ASM predictability following ENSO events and also explains why the predictive skill of the CFS_MAE prediction about two seasons ahead is comparable to that at 1-month lead as seen in Fig. 1.

In this study, we have concentrated on the effects of the ocean–atmosphere interactions on the ASM variability, prediction and predictability. It is noteworthy that, in comparison with observations, the loadings in the conventional EOF (MSN EOF) patterns of the hindcasts are generally smaller over the Asian continent than over its surrounding oceanic domain, similar to what Gao et al. (2011) have pointed out.

This may imply that the currently yielded ASM predictive skill (as seen in Fig. 1) is mainly associated with the successful prediction over ocean other than over land. How to improve the prediction of the ASM over the land is still a challenge the climate modeling community should pay attention to.

Acknowledgements This research is supported by Grants from NSF (AGS-1338427), NOAA (NA14OAR4310160), and NASA (NNX-14AM19G), and a grant from the Indian Institute of Tropical Meteorology and the Ministry of Earth Sciences, Government of India (MM/SERP/COLA-GMU_USA/2013/INT-2/002). We also acknowledge the Extreme Science and Engineering Discovery Environment (XSEDE) for providing the computational resources for the reforecast project. Finally, we thank two anonymous reviewers for their constructive comments and suggestions.

References

Achuthavarier D, Krishnamurthy V, Kirtman BP, Huang B (2012) Role of the Indian Ocean in the ENSO–Indian summer monsoon teleconnection in the NCEP climate forecast system. J Clim 25:2490–2508

Allen MR, Smith LA (1997) Optimal filtering in singular spectrum analysis. Phys Lett 234:419–428

Balmaseda MA, Vidard A, Anderson DLT (2008) The ECMWF ocean analysis system: ORA-S3. Mon Weather Rev 136:3018–3034. https://doi.org/10.1175/2008MWR2433.1

Balmaseda MA, Mogensen K, Molteni F, Weaver AT (2010) The NEMOVAR-COMBINE ocean re-analysis, COMBINE Tech. Rep No 1, 10 pp., Max Planck Inst. for Meteorol., Hamburg. http://www.combine-project.eu/fileadmin/user_upload/combine/tech_report/COMBINE_TECH_REP_n01.pdf

Behringer DW (2007) The global ocean data assimilation system at NCEP. In: Preprints, 11th symposium on integrated observing and assimilation systems for atmosphere, oceans and land surface, San Antonio, TX, American Meteor Society, pp 14–18

Cash BA, Barimalala R, Kinter JL, Altshuler EL, Fennessy M, Manganello J, Molteni F, Towers P, Vitart F (2017) Sampling variability and the changing ENSO-monsoon relationship. Clim Dyn 48:4071–4079. https://doi.org/10.1007/s00382-016-3320-3

Chowdary JS, Xie S-P, Lee J-Y, Kosaka Y, Wang B (2010) Predictability of summer Northwest Pacific climate in 11 coupled model hindcasts: Local and remote forcing. J Geophys Res 115:D22121. https://doi.org/10.1029/2010JD014595

Chowdary JS, Harsha HS, Gnanaseelan C, Srinivas G, Parekh A, Pillai P, Naidu CV (2017) Indian summer monsoon rainfall variability in response to differences in the decay phase of El Niño. Clim Dyn 48:2707–2727. https://doi.org/10.1007/s00382-016-3233-1

Du Y, Xie S-P, Huang G, Hu KM (2009) Role of air–sea interaction in the long persistence of El Nino–induced north Indian Ocean warming. J Clim 22:2023–2038

Gao H, Yang S, Kumar A, Hu Z-Z, Huang B, Li Y, Jha B (2011) Variations of the East Asian Mei-yu and simulations and prediction by the NCEP climate forecast system. J Clim 24(1):94–108. https://doi.org/10.1175/2010JCLI3540

Huang B (2004) Remotely forced variability in the tropical Atlantic Ocean. Clim Dyn 23:133–152

Huang R, Chen W, Yang B, Zhang R (2004) Recent advances in studies of the interaction between the East Asian winter and summer monsoons and ENSO cycle. Adv Atmos Sci 21:407–424

Huang B, Zhu J, Marx L, Wu X, Kumar A, Hu Z-Z, Balmaseda M, Zhang S, Lu J, Schneider EK, Kinter JL III (2015) Climate drift of AMOC, North Atlantic salinity and Arctic sea ice in CFSv2 decadal predictions. Clim Dyn 44:559–583. https://doi.org/10.1007/s00382-014-2395-y

Jiang X, Yang S, Li Y, Kumar A, Liu X, Zuo Z, Jha B (2013) Seasonal-to-interannual prediction of the Asian summer monsoon in the NCEP climate forecast system version 2. J Clim 26:3708–3727

Kang I-S, and Coauthors (2002) Intercomparison of the climatological variations of Asian summer monsoon precipitation simulated by 10 GCMs. Clim Dyn 19:383–395

Kim H-M, Webster PJ, Curry JA, Toma V (2012) Asian summer monsoon prediction in ECMWF system 4 and NCEP CFSv2 retrospective seasonal forecasts. Clim Dyn 39:2975–2991. https://doi.org/10.1007/s00382-012-1470-5

Kinter JL III, Miyakoda K, Yang S (2002) Recent change in the connection from the Asian monsoon to ENSO. J Clim 15:1203–1215

Kumar KK, Rajagopalan B, Cane MA (1999) On the weakening relationship between the Indian monsoon and ENSO. Science 284:2156–2159

Kumar KK, Hoerling M, Rajagopalan B (2005) Advancing Indian monsoon rainfall predictions. Geophys Res Lett 32:L08704. https://doi.org/10.1029/2004GL021979

Kumar KK, Rajagopalan B, Hoerling M, Bates G, Cane M (2006) Unraveling the Mystery of Indian monsoon failure during El Nino. Science. https://doi.org/10.1126/science.1131152

Kumar A, Chen M, Zhang L, Wang W, Xue Y, Wen C, Marx L, Huang B (2012) An analysis of the nonstationarity in the bias of sea surface temperature forecasts for the NCEP climate forecast system (CFS) version 2. Mon Weather Rev 140:3003–3016. https://doi.org/10.1175/MWR-D-11-00335.1

Lau N-C, Nath MJ (2000) Impact of ENSO on the variability of the Asian- Australian monsoons as simulated in GCM experiments. J Clim 13:4287–4309

Lau N-C, Nath MJ, Wang B (2004) Simulations by a GFDL GCM of ENSO-related variability of the coupled atmosphere-ocean system in the East Asian monsoon region. In: Chang CP (ed) East Asian monsoon, World Scientific, Mainland Press, Singapore, pp 271–300

Li CF, Lu RY, Dong BW (2012) Predictability of the western North Pacific summer climate demonstrated by the coupled models of ENSEMBLES. Clim Dyn 39:329–346

Liang JY, Yang S, Hu Z-Z, Huang B, Kumar A, Zhang Z (2009) Predictable patterns of the Asian and Indo-Pacific summer precipitation in the NCEP CFS. Clim Dyn 32:989–1001

Rajeevan M, Unnikrishnan CK, Preeth B (2012) Evaluation of the ENSEMBLES multi-model seasonal forecasts of Indian summer monsoon variability. Clim Dyn 38:2257–2274

Saha S, Coauthors (2010) The NCEP climate forecast system reanalysis. Bull Am Meteor Soc 91:1015–1057

Saha S, Coauthors (2014) The NCEP climate forecast system version 2. J Clim 27:2185–2208. https://doi.org/10.1175/JCLI-D-12-00823.1

Shin C-S, Huang B (2016) Slow and fast annual cycles of the Asian summer monsoon in the NCEP CFSv2. Clim Dyn 47:529–553. https://doi.org/10.1007/s00382-015-2854-0

Shin C-S, Huang B (2017) A spurious warming trend in the NMME equatorial pacific SST hindcasts. Clim Dyn. https://doi.org/10.1007/s00382-017-3777-8

Shukla J (1987) Interannual variability of monsoons. In: Fein JS, Stephens PI (eds) Monsoons, Wiley, New York, p 632

Shukla J, Paolino DA (1983) The Southern Oscillation and long range forecasting of the summer monsoon rainfall over India. Mon Weather Rev 111:18301837

Smith TM, Reynolds RW, Peterson TC, Lawrimore J (2008) Improvements NOAAs historical merged land–ocean temp analysis (1880–2006). J Clim 21:2283–2296

Venzke S, Allen MR, Sutton RT, Rowell DP (1999) The atmospheric response over the North Atlantic to decadal changes in sea surface temperature. J Clim 12:2562–2584
Wang B, Wu R, Fu X (2000) Pacific–East Asian teleconnection: How does ENSO affect East Asian climate? J Clim 13:1517–1536
Wang B, Wu R, Li T (2003) Atmosphere–warm ocean interaction and its impacts on Asian–Australian monsoon variation. J Clim 16:1195–1211
Wang B, Kang I-S, Lee J-Y (2004) Ensemble simulations of Asian–Australian monsoon variability by 11 AGCMs. J Clim 17:803–818
Wang B et al (2005) Fundamental challenge in simulation and prediction of summer monsoon rainfall. Geophys Res Lett 32:L15711. https://doi.org/10.1029/2005GL022734
Wang B, Yang J, Zhou T, Wang B (2008) Interdecadal changes in the major modes of Asian-Australian monsoon variability: strengthening relationship with ENSO since the late 1970s. J Clim 21:1771–1789
Wang B et al (2009) Advanced and prospectus of seasonal prediction: assessment of the APCC/CliPAS 14-model ensemble retrospective seasonal prediction (1980–2004). Clim Dyn 33:93–117
Wang B, Lee J-Y, Xiang B (2015) Asian summer monsoon rainfall predictability: a predictable mode analysis. Clim Dyn 44:61–74. https://doi.org/10.1007/s00382-014-2218-1
Wang B, Li J, He Q (2017) Variable and robust East Asian monsoon rainfall response to El Niño over the past 60 years (1957–2016). Adv Atmos Sci 34:1235–1248
Webster PJ, Yang S (1992) Monsoon and ENSO: selectively interactive systems. Q J R Meteor Soc 118:877–926
Webster PJ, Magaña VO, Palmer TN, Thomas RA, Yanai M, Yasunari T (1998) Monsoons: processes, predictability, and the prospects for prediction. J Geophys Res 103:14451–14510
Webster PJ, Moore AM, Loschnigg JP, Leben RR (1999) Coupled oceanic-atmospheric dynamics in the Indian Ocean during 1997–1998. Nature 401:356–360
Winton M (2000) A reformulated three-layer sea ice model. J Atmos Ocean Technol 17:525–531
Wu R, Hu Z-Z, Kirtman BP (2003) Evolution of ENSO-related rainfall anomalies in East Asia. J Clim 16(22):3742–3758
Wu Z, Li J, Jiang Z, He J, Zhu X (2012) Possible effects of the North Atlantic Oscillation on the strengthening relationship between the East Asian summer monsoon and ENSO. Int J Climatol 32:794–800. https://doi.org/10.1002/joc.2309
Xavier PK, Marzin C, Goswami BN (2007) An objective definition of the Indian summer monsoon season and a new perspective on the ENSO-monsoon relationship. Q J R Meteor Soc 133:749–764
Xiang BQ, Wang B, Yu WD, Xu SB (2013) How can anomalous western North Pacific subtropical high intensify in late summer? Geophys Res Lett 40:2349–2354
Xie P, Arkin PA (1997) Global precipitation: a 17-year monthly analysis based on gauge observations, satellite estimates, and numerical outputs. Bull Am Meteor Soc 78:2539–2558
Xie S-P, Philander SGH (1994) A coupled oceanatmosphere model of relevance to the ITCZ in the eastern Pacific. Tellus. https://doi.org/10.1034/j.1600-0870.1994.t01-1-00001.x
Xie S-P, Annamalai H, Schott FA, McCreary JP Jr (2002) Structure and mechanisms of South Indian Ocean climate variability. J Clim 15:864–878
Xie S-P, Hu K, Hafner J, Du Y, Huang G, Tokinaga H (2009) Indian Ocean capacitor effect on Indo-western Pacific climate during the summer following El Niño. J Clim 22:730–747
Xie S-P, Kosaka Y, Du Y, Hu K, Chowdary JS, Huang G (2016) Indo-western Pacific Ocean capacitor and coherent climate anomalies in post-ENSO summer: a review. Adv Atmos Sci 33:411–432
Xue Y, Huang B, Hu Z-Z, Kumar A, Wen C, Behringer D, Nadiga S (2011) An assessment of oceanic variability in the NCEP climate forecast system reanalysis. Clim Dyn 37:2511–2539. https://doi.org/10.1007/s00382-010-0954-4
Xue Y, Chen M, Kumar A, Hu Z-Z, Wang W (2013) Prediction skill and bias of tropical Pacific sea surface temperatures in the NCEP climate forecast system version 2. J Clim 26:5358–5378. https://doi.org/10.1175/JCLI-D-12-00600.1
Yang S, Jiang X (2014) Prediction of eastern and central Pacific ENSO events and their impacts on East Asian climate by the NCEP climate forecast system. J Clim 27:4451–4472
Yang S, Lau K-M (2006) Interannual variability of the Asian monsoon. In: Wang B (ed), The Asian Monsoon, Praxis, Chennai, pp 259–293
Yang S, Zhang Z, Kousky VE, Higgins RW, Yoo S-H, Liang J, Fan Y (2008) Simulations and seasonal prediction of the Asian summer monsoon in the NCEP climate forecast system. J Clim 21:3755–3775
Yu L, Jin X, Weller RA (2008) Multidecade Global flux datasets from the objectively analyzed air–sea fluxes (OAFlux) project: latent and sensible heat fluxes, ocean evaporation, and related surface meteorological variables. Woods Hole Oceanographic Institution, OAFlux Project Technical Report. OA-2008-01, pp 64, Woods Hole, Massachusetts. http://oaflux.whoi.edu/pdfs/OAFlux_TechReport_3rd_release.pdf
Yun KS, Seo KH, Ha KJ (2010) Interdecadal change in the relationship between ENSO and the intraseasonal oscillation in East Asia. J Clim 23:3599–3612
Zhang W, Jin F-F, Stuecker MF, Wittenberg AT, Timmermann A, Ren H-L, Kug J-S, Cai W, Cane M (2016) Unraveling El Niño's impact on the East Asian Monsoon and Yangtze River summer flooding. Geophys Res Lett 43, 11,375–11,382. https://doi.org/10.1002/2016GL071190
Zhang T, Huang B, Yang S, Laohalertchai C (2018) Seasonal dependence of the predictable low-level circulation patterns over the tropical Indo-Pacific domain. Clim Dyn. https://doi.org/10.1007/s00382-017-3874-8
Zheng Z, Hu Z-Z, L'Heureux M (2016) Predictable components of ENSO evolution in real-time multi-model predictions. Sci Rep 6:35909. https://doi.org/10.1038/srep35909
Zhu J, Huang B, Balmaseda MA (2012a) An ensemble estimation of the variability of upper-ocean heat content over the tropical Atlantic Ocean with multi-ocean reanalysis products. Clim Dyn 39:1001–1020. https://doi.org/10.1007/s00382-011-1189-8
Zhu J, Huang B, Marx L, Kinter JL, Balmaseda III,MA, Zhang R-H, Hu Z-Z (2012b) Ensemble ENSO hindcasts initialized from multiple ocean analyses. Geophys Res Lett 39:L09602. https://doi.org/10.1029/2012GL051503
Zhu J, Huang B, Balmaseda MA, Kinter JL, Peng III,P, Hu Z-Z, Marx L (2013) Improved reliability of ENSO hindcasts with multi-ocean analyses ensemble initialization. Clim Dyn 41:2785–2795. https://doi.org/10.1007/s00382-013-1965-8
Zuo Z, Yang S, Hu Z-Z, Zhang R, Wang W, Huang B, Wang F (2013) Predictable patterns and predictive skills of monsoon precipitation in Northern Hemisphere summer in NCEP CFSv2 reforecasts. Clim Dyn 40:3071–3088. https://doi.org/10.1007/s00382-013-1772-2